Optical emission and nanoparticle generation in Al plasmas using ultrashort laser pulses temporally optimized by real-time spectroscopic feedback

M. Guillermin,[1] J. P. Colombier,[1] S. Valette,[2] E. Audouard,[1] F. Garrelie,[1,*] and R. Stoian[1,†]
[1]*Laboratoire Hubert Curien, UMR CNRS 5516, Université de Lyon, Université Jean Monnet, 42000 Saint-Etienne, France*
[2]*Laboratoire de Tribologie et Dynamique des Systémes, UMR CNRS 5513, École Centrale de Lyon, 69134 Écully, France*
(Received 9 November 2009; revised manuscript received 26 May 2010; published 20 July 2010)

With an interest in pulsed laser deposition and remote spectroscopy techniques, we explore here the potential of laser pulses temporally tailored on ultrafast time scales to control the expansion and the excitation degree of various ablation products including atomic species and nanoparticulates. Taking advantage of automated pulse-shaping techniques, an adaptive procedure based on spectroscopic feedback is applied to regulate the irradiance and enhance the optical emission of monocharged aluminum ions with respect to the neutral signal. This leads to optimized pulses usually consisting in a series of femtosecond peaks distributed on a longer picosecond sequence. The ablation features induced by the optimized pulse are compared with those determined by picosecond pulses generated by imposed second-order dispersion or by double pulse sequences with adjustable picosecond separation. This allows to analyze the influence of fast- and slow-varying envelope features on the material heating and the resulting plasma excitation degree. Using various optimal pulse forms including designed asymmetric shapes, we analyze the establishment of surface pre-excitation that enables conditions of enhanced radiation coupling. Thin films elaborated by unshaped femtosecond laser pulses and by optimized, stretched, or double pulse sequences are compared, indicating that the nanoparticles generation efficiency is strongly influenced by the temporal shaping of the laser irradiation. A thermodynamic scenario involving supercritical heating is proposed to explain enhanced ionization rates and lower particulates density for optimal pulses. Numerical one-dimensional hydrodynamic simulations for the excited matter support the interpretation of the experimental results in terms of relative efficiency of various relaxation paths for excited matter above or below the thermodynamic stability limits. The calculation results underline the role of the temperature and density gradients along the ablated plasma plume which lead to the spatial distinct locations of excited species. Moreover, the nanoparticles sizes are computed based on liquid layer ejection followed by a Rayleigh and Taylor instability decomposition, in good agreement with the experimental findings.

DOI: 10.1103/PhysRevB.82.035430 PACS number(s): 52.38.Dx, 42.25.Bs, 05.70.Ln, 79.20.Ds

I. INTRODUCTION

Rapid development in ultrafast laser technologies during last decades has been accompanied by an intense research activity concerning the control and the understanding of laser-induced ultrafast processes. The femtosecond laser pulse allows the confinement of electromagnetic energy deposition in space and time. This strong localization of the interaction reduces the energy expense of ablation and limits the thermally affected area.[1,2] The fast quasi-isochoric heating produced by femtosecond laser pulses pushes the irradiated material in extreme thermodynamical states. At sufficient energy, high heating rates allow the onset of supercritical relaxation paths for the superficial layers and the corresponding ablation mechanisms can be assigned to an atomization or fragmentation of the hot fluid.[3,4] As the distribution of the deposited energy density is nonuniform, the deeper layers undergo other ablation mechanisms involving crossing thermodynamics boundaries into the gas-liquid cohabitation zone. Strong pressure wave generation associated with the material expansion induces the decomposition and the ejection of the metastable matter through ablation processes described in terms of phase explosion.[5–8] Lastly, deep molten layers decay along the binodal in a dominantly liquid phase subject to capillary forces and forming the recast.

The confinement of energy deposition associated to femtosecond laser irradiation is critical for applications such as micromachining,[1] laser-induced forward transfer,[9,10] or laser-induced breakdown spectroscopy (LIBS),[11,12] through phenomena that include localized removal, shock wave generation, or limitation of the target damage extent. The nonlinear properties of ultrashort laser pulses propagation allow as well the development of long-distance applications such as remote spectroscopy for atmospheric analysis.[13] In the typical ablation regimes, the high kinetic energy of the ablated species in the plasma plume permits the production through pulsed laser deposition (PLD) techniques of thin films with low residual stress[14–16] and conservation of target stoichiometry.[17] Among the new possibilities opened by the capability of femtosecond pulses to induce nonequilibrium and extreme states in the irradiated solid, direct nanoparticles ejection is one of the most striking characteristics of ultrashort laser ablation.[18–20] In addition, critical states allow the onset of specific thermodynamics condition for gas-phase condensation of nanoparticles.[21] This particular effect of femtosecond laser ablation offers a new path to elaborate nanostructured thin films by PLD.[22–24]

The efficiency of the PLD process is related to the ability to control the ablation plume characteristics such as composition, excitation, reactivity, and kinetic properties of species, or generation of particulates. In particular, the understanding and the control of the nanoparticles generation processes subsequent to femtosecond laser irradiation are very promising topics in terms of fundamental research and technologi-

cal applications. The ablation products characteristics can be influenced through parameters such as laser wavelength, pulse duration, laser fluence, laser spot size, substrate temperature, or residual pressure. For example, recent studies report the analysis of nanoparticles production according to these parameters,[25–28] indicating a potential control of nanoparticles surface density and size distributions. The challenge is to obtain improved and controllable throughputs with minimal energy and material costs.

A promising approach of the laser-matter interaction control consists in the modification of the energy deposition rate through the temporal tailoring of laser pulses on ultrafast time scales. A simple version involves laser systems delivering pulses of different durations by dispersion control on the compression stage or interferometric setups to generate double pulses (DPs) sequences. These techniques have been applied to improve processes such as laser microfabrication of metals,[29–35] dielectrics,[33,36,37] or semiconductors,[33,37–39] LIBS[12,33,40–44] and PLD.[45–47] With the advent of automated pulse-shaping techniques, the phase modulation deriving from spectral filtering of femtosecond laser pulses[48] and the associated effect in the temporal domain allow to define more complex temporal shapes which can be efficiently used to optimize processing or material transfer applications.[49–51] Moreover, in view of the complexity of the laser ablation process, these programmable techniques allow the implementation of improvement loops and advanced optimization procedures, making possible new interaction paths and increased synergies between light and matter.

In this context, the temporal distribution of the laser irradiation on ultrafast time scales becomes a key parameter for controlling ablation scenarios. Usually several modeling and numerical simulation studies are used to bring determinant elements toward understanding phenomena underlying femtosecond laser ablation.[8,52,53] Nevertheless, the analytical definition of adapted temporal shapes of laser pulses for particular optimization purposes, such as control of the plasma plume excitation and ionization state or influence on the nanoparticles generation, remains a challenge due to the many intermediate and complex phases between excitation and ablation. To overcome these theoretical limitations, it is often of advantage to actively couple the experimental characterization device with the pulse envelope control unit [e.g., based on spatial light modulators (SLMs)[48]] in a loop driven by self-adapting procedures (e.g., learning evolutionary algorithm). Initially applied in the field of femtochemistry,[54–57] those adaptive procedures have recently been used to improve femtosecond laser ablation processes. The yield of ions production during the ablation of silicon and the laser energy coupling to an aluminum target have been optimized using a feedback based on time-of-flight mass spectrometry (MS-TOF).[6,58,59] The second-harmonic generation signal has been used to characterize and optimize pulses for machining[60] while the generation of nanoparticles process has been influenced by using additionally an electrical low-pressure cascade impactor.[61]

The study reported in this paper is focused on the control of femtosecond laser ablation of aluminum in the fluence range usually employed in LIBS and PLD applications. Following the approach reported in a previous study (Ref. 6) devoted to the optimization of the energy coupling into an aluminum target at more moderate laser fluence (typical for precise machining applications) based on a MS-TOF signal feedback, we aim here at influencing the ablation and plasma generation processes through an adaptive procedure of optimization based on the spectral measurement of the plasma plume optical emission corresponding to various atomic constituents. This is also motivated by the fact that spectral detection is largely employed in PLD studies. This work attempts thus to control the excitation and ionization state of the ablated material through a suited temporal tailoring of the femtosecond pulses. Such a control on ablation properties could influence the plasma reactivity and the particulates generation, having far reaching consequences for applications. Optimization effects on plasma excitation and ionization states and on final ablation products could in turn be characterized and linked to specific thermodynamic scenarios. The influence of temporally optimized pulses on ablation results is successfully reproduced here by numerical simulations providing elements to correlate temporal features of pulse shapes and physical ablation mechanisms induced by the irradiation. A particular interest is dedicated to nanoparticles generation.

The paper is divided in several sections. The following section describes the experimental device while Sec. III exposes the numerical simulation method of the material thermodynamic evolution which is based on a hydrodynamic approach. Section IV is devoted to the experimental and simulation results concerning the plasma optical-emission behavior deriving from the optimization of the laser-pulse temporal shapes. A discussion about the mechanisms leading to additional plume excitation correlated with the sequence of optical transients and phase changes is presented. Section V presents an analysis of the influence the optimized pulses exercise on nanoparticles generation.

II. EXPERIMENTAL SECTION

The experimental setup used in this study is depicted in Fig. 1 and it is based on two main elements. The radiation source is a femtosecond laser system with time-tailorable pulses irradiating a solid aluminum sample. The apparatus is completed by a detection and evaluation unit based on spectroscopic analysis of the laser-induced plasma optical emission.

The amplified femtosecond laser system delivers 150 fs full width at half maximum (FWHM), 1 mJ, *p*-polarized pulses with a wavelength centered at 800 nm. The repetition rate is controlled externally in the range 0.1 Hz to 1 kHz. The laser radiation is focused onto a pure aluminum rotating target (99.9%) in a vacuum chamber ($P \sim 10^{-5}$ Pa) through a 500 mm focal length lens. The incidence angle with respect to the target surface normal is 45°. The average fluence is estimated through recurrent measurements of the impact region surface at various energies[62] and is kept around the value of 5.8 J/cm^2 (more than one order of magnitude larger than the macroscopic ablation threshold[63] evaluated at 0.3 J/cm^2 in good agreement with previous reports in the literature[5,31,64]).

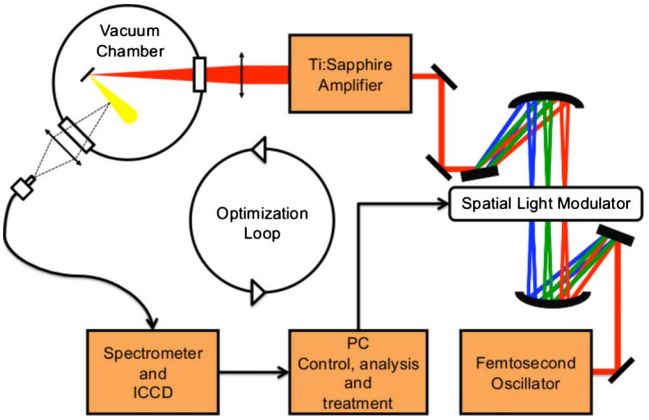

FIG. 1. (Color online) Illustration of the irradiation and acquisition setup. Sketch of the feedback loop based on spectral detection.

The irradiation system incorporates a pulse tailoring unit in the time domain, relying on spectral filtering of pulse frequency components in dispersive systems.[48] The phase of laser pulses is modulated prior amplification using a SLM based on a pixelated liquid crystals array. The 640 pixels array allows a high spectral resolution and a shaping window superior to 20 ps. This device realizes a complex phase-only filtering and permits to achieve the temporal shaping of the femtosecond laser pulse while preserving the total energy in the sequence. Eventual spatial distortions are eliminated by the postshaping amplification process. Intensity temporal distributions of laser pulses are then determined by background-free second-order nonlinear intensity cross correlation between a Fourier-limited reference femtosecond pulse and the shaped pulse.

The time-resolved spectroscopic analysis of the light emitted by the plasma is performed by a UV-VIS spectrometer (Chromex) connected to a fast-gated intensified charge-coupled device (ICCD) camera (Hamamatsu). All spectra presented in this paper are recorded for an acquisition delay of 100 ns after the laser impact and with a time gate of 300 ns and averaged over 45 pulses. These parameters have been chosen in order to maximize the acquired intensity and integrate the different rapid dynamics of several spectral lines. This is required to monitor both neutral and ionic signals in the same acquisition run. The speed of the rotating target (4.5 rad/s) is chosen to avoid as good as possible overlapping between acquisition pulses. The target is previously irradiated with an average of five pulses per site to ensure an optimal cleaning of the material surface. The consequence is a slight corrugation of the surface in form of ripples which represent a deviation from a planar geometry. The experimental device was described in detail elsewhere.[51] Returning to the detection apparatus, on the nanosecond time scale, the plasma optical emission is spatially integrated (the collection region being 25.4 mm wide, centered on the target surface) but the information is derived mainly from the dense regions of the plume. The potential influence of the spatial and temporal integrations on the results is discussed in Sec. IV. The ICCD camera is also punctually used to perform direct imaging of the plasma, allowing to investigate the expansion geometry of the ablated matter.

TABLE I. Aluminum spectroscopic lines associated with their parameters (A_{ki} the transition probability, E_k the upper-level energy, and g_k the multiplicity of the upper level) extracted from Ref. 65.

Species	Wavelength (nm)	A_{ki} (s^{-1})	E_k (eV)	g_k
Al II (a)	281.7014	3.83×10^8	11.82197	1
Al I (b)	308.21529	6.3×10^7	4.0214834	4
Al I (c)	309.27099	7.4×10^7	4.0216499	6
	309.28386	1.2×10^7	4.0214834	4
Al II (d)	358.6557		15.302545	9
	358.6708		15.302545	9
	358.6811		15.302545	9
	358.6912		15.302185	7
	358.7068		15.302185	7
	358.7165		15.30194	5
	358.7309		15.30194	5
	358.7450		15.30194	5
Al I (e)	394.40058	4.93×10^7	3.142721	2
Al I (f)	396.15200	9.8×10^7	3.142721	2
Al II (g)	466.3056	5.3×10^7	13.256459	3
Al II (h)	559.3302	1.1×10^8	15.472499	5
Al II (i)	623.162	4.7×10^7	15.0621266	3
	623.1750	8.4×10^7	15.062085	5
Al II (j)	624.307	3.1×10^6	15.0621266	3
	624.320	2.8×10^7	15.062085	5
	624.337	1.1×10^8	15.062033	7
Al II (k)	704.206	5.9×10^7	13.076728	5
Al II (l)	705.660	5.8×10^7	13.073079	3

The programmable nature of the SLM allows its insertion into a computer controlled optimization loop relying on the feedback delivered by the spectroscopic tool. In view of the complexity of the ablation process, the irradiation-detection loop is driven by an adaptive approach. The optimization procedure is based on an evolutionary strategy and is used to progressively adapt the temporal shape of the laser pulse to induce a particular user-defined result recorded by the ablation characterization device. As compared to the previous study on optimizing kinetic parameters of the ablation products via mass spectrometry,[6] this spectral emission approach gives direct access to the excitation state of the plume allowing to influence emission features. Table I summarizes the lines studied in this work and their spectroscopic characteristics.[65,66] The Al-II transitions at 358.7 nm [with the label (d) in Table I] are chosen to monitor the ionic emission while the two Al-I lines [(e) and (f)] at 394.4 and 396.15 nm provide information on the neutral population. The difference between these ionic and neutral lines intensity (respectively, I^d for Al-II, I^e and I^f for Al-I) indicates the relative state of ionization of the plasma plume and is used to quantify the efficiency of a particular temporal shape to enhance the ionization degree of the ablated matter. This quantity,

$$f = I^d - I^e - I^f, \quad (1)$$

playing the role of the fitness parameter, guides the numerical adaptive procedure.[51]

The adaptive procedure is applied to lock up temporal shapes that maximize the fitness value. Detailing this procedure, an initial group of temporal shapes randomly defined is ranked with respect to the generated fitness value. The best shapes are then selected and genetic propagators, mimicking biological evolution (with processes such as crossover and mutation), are applied in the Fourier spectral domain to define a new group of temporal shapes for laser pulses. This process is iteratively reproduced until a satisfying optimization level is achieved. Because of the time-consuming character of the evolutionary procedure, the integration for each acquisition during the optimization process is set to 15 laser pulses (the final result is then acquired with 45 pulses per acquisition). Moreover, this allows to limit the erosion of the target with a maximum of ten pulses per site.

In order to study the temporal shaping effect on the thin-film deposition process, pure silicon (100) substrates are positioned in the vacuum chamber in front of the aluminum target surface at a distance of 38 mm to collect ablation products. All deposited layers mentioned in this article are realized with 15-min-long irradiation at 1 kHz on separate sample areas and the achieved surface morphology is characterized using a mechanical profilometer and a scanning electron microscope equipped with a field-emission gun (FEG-SEM).

III. SIMULATION OF THERMODYNAMIC EVOLUTION

To accompany the experimental approach, we have performed the simulation of the nonequilibrium heating and expansion of an aluminum sample irradiated by an ultrashort or a temporally-shaped laser pulse using a one-dimensional two-temperature hydrodynamic code (Esther).[4] We are interested in the thermal and kinetic properties of the plume at the end of the irradiation sequence. The utilized approach solves, according to a Lagrangian scheme, the fluid equations for the conservation of mass, momentum and energies for electronic and ionic species.[4] The thermodynamic properties of the material (energy, temperature, pressure, density, heat of fusion, and vaporization) are described by the Bushman-Lomonosov-Fortov multiphase equation of state (EOS) that encompasses a large range of densities and temperatures starting from cold condensed state and down to the hot plasma.[67] This EOS provides the evolution of the thermodynamic properties and has already been applied to determine paths followed by the excited matter and even to characterize the nonequilibrium laser interaction process.[6,68] In a first step, the interaction between the laser field and the target is calculated by solving the Helmholtz wave equation in the inhomogeneous media. This requires accurate values for the spatially varying conductivity through the Drude model. We used the values from Ref. 69 in the solid phase while in the plasma phase we have used corresponding values from Ref. 70 and, at lower densities, the Spitzer formula.[71] The model describing the ultrashort absorption was discussed in more details elsewhere[72] and represents an upgrade from the model used previously (Ref. 6) by including additional contribution to absorption such as umklapp electronic collisions, a matter still under debate. For longer pulses, because of the formation of a density gradient in front of the target due to the hydrodynamic expansion, shielding occurs and the laser beam is partially absorbed before it reaches the dense part of the target. As coupling into the expanding matter is an important factor, the laser energy can be considerably attenuated before it reaches the unperturbed part of the target, leading to less efficient heating of the solid material. The total amount of matter which undergoes melting and vaporization is then reduced and the emphasis is moved to plasma evolution. The energy sequence delivered by the shaped pulse during the initial expansion stages determines the plasma states reached by the ablated Al target. Laser radiation is absorbed primarily by inverse Bremsstrahlung through electron-electron, electron-phonon, electron-neutral, and electron-ion collisions, having the consequence that the electron is raised to a higher state in the continuum. Photoionization of excited states contributes only for energetic photons impinging on easily ionized gas mixtures and it is neglected here.

Laser heating of metals can be modeled by four basic processes: the deposition of radiation energy on free electrons, the energy exchange between electrons and lattice, the diffusion of energy through media by free-electron motion, the heating and the conversion to mechanical energy by formation and propagation of shock waves. In the course of ultrashort laser heating, where the metal is looked upon as a two-temperature system, the free electrons are heated to an effective temperature much higher than that of the lattice. This imposes to include the two-temperature model in our numerical approach to address the nonequilibrium processes (Ref. 73) and the large local temperature differences between the electrons and the lattice. Subsequently, the transport of energy from the electrons to the lattice takes place by means of an electronic thermal-conduction mechanism. A coupling coefficient $\gamma(T_e, n_e)$ between the electron and phonon subsystems is considered. The relaxation mechanism is crucial in this work and we have taken a special care to describe the coupling coefficient in a realistic manner. With respect to Ref. 6 and considering the argumentation in Ref. 74, the dependence on electronic properties has been determined here by $\gamma(T_e, n_e) = \gamma^0(T_e) \times (n_e/n_e^0)^{1/3}$, where n_e^0 is the electronic density in the initial solid state and $\gamma^0(T_e)$ the electron-phonon coupling coefficient at solid density. We assume that this energy equilibration rate in nonequilibrium electron-ion systems remains valid for a large class of ionic configurations including solid and liquid metals phases, as well as warm dense matter. For the dilute, hot, and therefore weakly coupled plasmas for which the thermal energy of the particles greatly exceeds the potential energies, the energy relaxation among electrons and ions is taken into account based on the usual Spitzer model including the Coulomb logarithm. Two *ad hoc* cutoff parameters are used in this approach to mimic the quantum interference and finite-ion-size effects for short-distance collisions as well as the Coulomb screening of the charges.[75,76] Between the regimes of warm dense matter and weakly coupled, nondegenerated plasmas, we have used a polynomial interpolation to connect

both models for densities lower than the critical one.

For each time step and cells of the Lagrangian simulation, the number of free electrons is connected to the number of ions by the relation $n_e = Z^\star n_i$, where $Z^\star$ is the average ionization. The data for the ionization state calculated within a generalized chemical model in a wide range of densities and temperatures are taken from the Ref. 70. In these tabulated data, the density varies from 1 to 10^5 Kg m^{-3} while the temperature ranges from 10^2 to 10^8 K. For lower densities, from 10^{-5} to 1 Kg m^{-3}, we have used the data calculated by Refs. 77 and 78 which are in agreement with recent ionization data for Al discussed in the literature.[79] These values are calculated for electrons and ions at equilibrium but we assume that the ionization is mainly determined by the electronic collisions and we have used the equilibrium values of average ionization for $T=T_e$, the electronic temperature. During the electron-ion relaxation stage, $Z^\star$ is modified along the T_e decrease and a kind of numerical recombination process occurs. To convert this process in energy recombination and to avoid an effect of T_e increase due to a drop of n_e, we have added an energy exchange term in the form

$$\frac{\partial \varepsilon_e}{\partial t} = \frac{n_e \zeta_e}{Z^\star}\frac{\partial Z^\star}{\partial t} = -\frac{\partial \varepsilon_i}{\partial t}, \tag{2}$$

where ε_i is the equilibrium matter energy, $\varepsilon_e = \zeta_e n_e$ is the energy of the electron subsystem, and ζ_e the average energy of a particle.

This numerical approach is used to simulate the ablation phenomena and related effects induced by laser pulses temporally shaped on ultrafast time scales. To assist the interpretation of experimental results concerning the plasma optical emission and the particulates generation, we attempt to follow the thermodynamics conditions reached by the ejected material from the initial energy deposition until longer times, typically hundreds of nanosecond. Nevertheless, the numerical approach is limited to a one-dimensional simulation of the expansion plume whereas three-dimensional approaches are desirable for simulating the later plume expansion stages. A direct layering to the experimental results is therefore not accurate and a quantitative interpretation must be done with precaution. Usually, 1D hypothesis is limited to expansion of size similar to the irradiation zone. Nevertheless, in usual PLD conditions where cm scales are typically involved for collecting the material, we can notice that the ablated matter is deposited on a surface about 10^4 higher than the focal spot, and that one can expect densities of the plasma up to 10^4 weaker than the one simulated at 3 cm of the target because of the lateral expansion. While supposing that the 1D temperature remains correct, the ionization rate appears to be not very sensitive to such a decrease in density and the tables provide an ionization increase of less than 5%. Consequently, we can reasonably suppose that our approach remains suitable to support in a qualitative manner our results.

IV. PLASMA OPTICAL EMISSION

The first part of discussion concerns plasma emissivity. We present below the experimental results concerning the optimization of plasma optical emission with respect to the excitation degree through the tailoring of the laser energy temporal distribution on ultrafast time scales. As indicated, the excitation degree of the species in the plume and the relative concentration of species are supposed to determine to a large extent the reactivity of the plasma. We used the setup described in Sec. II to enhance the ionic emission of plasma with respect to the light emitted by neutral species. The experimental results are compared with numerical simulations of plasma plume allowing to discuss physical mechanisms involved in the specific response of thermodynamic states of aluminum to the temporal tailoring of energy deposition.

A. Experimental results

The adaptive approach driving the presented loop was applied in order to determine the ablation plasma characteristics in specific spectral domains. The use of the evolutionary optimization procedure permits to modify the emission (recorded between 100 and 400 ns after laser exposure) of transitions considered in the fitness parameter defined in the Eq. (1), hence leading to optimal shaped pulses. According to our definition, this induces an enhancement of the Al-II lines intensity [multiplet (d) at 358.7 nm] and a reduction in emission for the Al-I transitions [multiplets (e) at 394.4 and (f) at 396.15 nm]. Figure 2(a) shows the comparison between spectral intensities induced in the spectral domain used for the optimization by a femtosecond short pulse (SP) and those of the optimized pulses (OP). The cross-correlation measurement of the short and optimized-pulse temporal shapes is depicted in Figs. 2(b) and 2(c). The OP sequence consists of a series of peaks (separated by 1 or 2 ps) superposed onto a stretched distribution (Gaussian envelop of 6 ps FWHM). However, the OP solution is not unique within the sensitivity of the experiment. A second optimal irradiation sequence OP′, fulfilling the optimization requirements, is presented in Fig. 2(d) and will be used later in the text to define the topology of the search space and the requirements for emission improvements (see Sec. IV D). The following discussion is mainly based on the OP sequence but is pertinent for a large range of pulse shapes that perform similarly in the optimization run. To describe the observed influence of the temporally tailored energy deposition on the plasma optical emission, we define the multiplication factor,

$$M^i_{\mathrm{XP}} = \frac{I^i_{\mathrm{XP}}}{I^i_{\mathrm{SP}}} \tag{3}$$

corresponding to the intensity modification of a particular transition i with a given shaped pulse with respect to the unshaped femtosecond short pulse. The relative increase in the integrated intensity emitted by singly charged aluminum ions (Al-II) is then given by $M^d_{\mathrm{OP}} = 3.2 \pm 0.4$ when OP is applied. Intensities of the two neutral lines used as feedback for Al-I atoms are reduced according to $M^e_{\mathrm{OP}} = 0.54 \pm 0.07$ and $M^f_{\mathrm{OP}} = 0.59 \pm 0.07$. To be further used in the analysis, excitation temperature are evaluated through the Boltzmann ratio intensity method[80] with transitions [(b) and (e)] for neutral aluminum atoms (Al-I) and [(h) and (l)] for aluminum ionized one time (Al-II). The precision of this method is

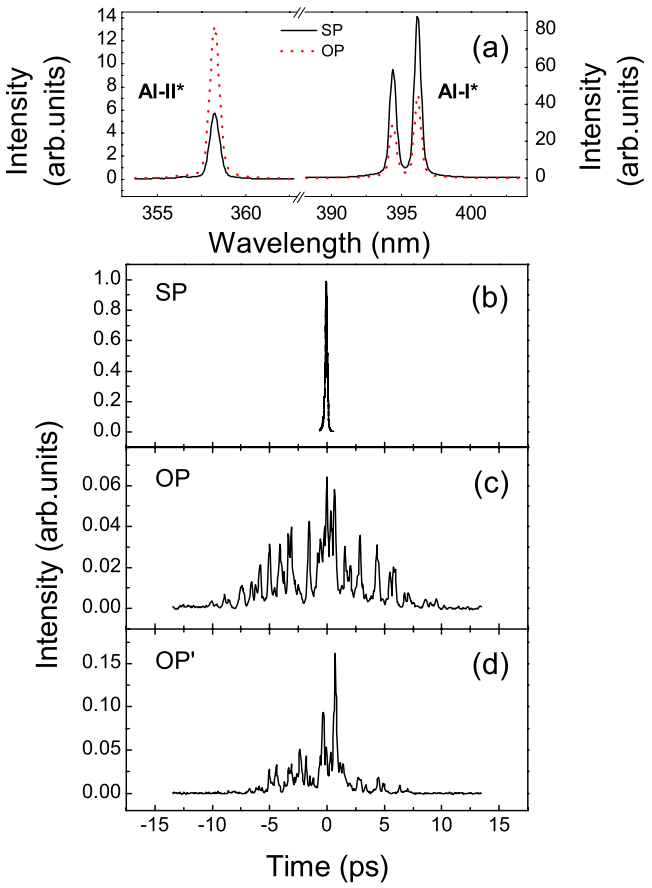

FIG. 2. (Color online) (a) Spectral intensity of the lines involved in the optimization process indicating Al-I and Al-II emission after irradiation induced with short and optimized pulses (respectively, SP and OP). Temporal distribution of the intensity for SP (b) and several optimal forms OP (c) and OP′ (d) determined by cross correlation (see text for details).

nevertheless strongly limited by the spatiotemporal integration of the emission line intensity measurements in case of the rapidly varying plume. Only rough estimates can be made and will be used to indicate qualitative tendencies upon different excitation situations. The excitation temperature induced with femtosecond pulses SP or with optimized pulses OP are quite similar for both species, approximately 5000 K for Al-I and 20 000 K for Al-II. The overall intensity summed respectively for all Al-I and Al-II transitions are modified as follows: $M_{\mathrm{OP}}^{\mathrm{Al\text{-}I}}=0.56\pm0.07$ and $M_{\mathrm{OP}}^{\mathrm{Al\text{-}II}}=2.9\pm0.4$ with a similar trend as described for (d), (e), and (f) lines. The global intensity emitted by all the transitions listed in the Table I and corresponding to the plasma luminosity is reduced with a factor $M_{\mathrm{OP}}^{tot}=0.76\pm0.09$. We can now compare the fractions emitted by Al-II or Al-I. The femtosecond SP leads to a repartition of the overall studied emission consisting of 91% of total intensity emitted by Al-I and 9% by Al-II while optimized pulse OP induces a fraction of 68% for neutrals emission and 32% for Al-II atoms.

In order to complete the experimental investigations of the plasma behavior, we perform direct imaging of the ablation plume in the UV-VIS spectral range at different time delays after the laser impact. Figure 3 shows images of the

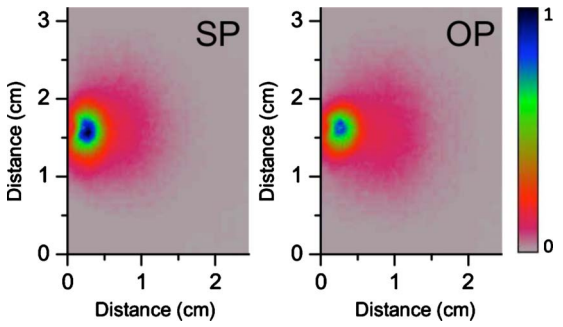

FIG. 3. (Color online) Plasma images in the UV-VIS domain (from 200 to 800 nm) recorded at 300 ns delay after laser exposure for a gate integration time of 100 ns. The intensity is accumulated over ten laser pulses and comes mainly from neutral emission with slight ionic contributions expanding ahead (see text).

optical plasma emission induced by short and optimized pulses for an evolution gated between 300 and 400 ns. The intensity is integrated over ten successive laser pulses. At the usual fluence, the plasma consists dominantly on neutrals emitting in visible and ions in ultraviolet. We note that the SP-induced optical emission is more intense than the one generated with optimized pulses as it originates mainly from the dominant neutral emission. The extension of the plasma plume is slightly larger with OP than with SP exposure. Additionally, the corresponding ablation rates were evaluated through *ex situ* profilometry measurements of ablation craters. The ablation rate is higher with the short pulse (98 ± 1 nm/pulse) than with the optimized irradiation sequence (80 ± 4 nm/pulse) at the 5.8 J/cm^2 incident fluence. However, considering that not all the ablated material is transported into the gas phase as it will be seen later, it is difficult to make correlations between the plumes only based on the ablation rates.

B. Simulation of temperature-density-ionization profiles

Building on the initial results presented in Ref. 6 that estimate the kinetic plasma properties, we focus here on its thermal characteristics. The numerical simulations described in the Sec. III are used to compute the spatial profiles of density $n(z)$ and temperature $T(z)$ of ablated aluminum 250 ns after the moment of energy deposition (initial solid surface at $z=0$) in a one-dimensional approach. Here z is the expansion direction. At this time, the plume is already equilibrated. The inherent limitation of the 1D approach in attempting a full description of plume evolution was previously indicated (see Sec. III). The mean ionization rate Z^* (in e^-/atom) is used in a tabulated form,[77] with respect to density and temperature. The electronic density n_e can be written as

$$n_e=\sum_{k=1}^{k_{\max}} kn_k=Z^*n(z) \tag{4}$$

with n_k the density of atoms in the k ionized state and $k_{\max}=13$. Assuming that the Saha equation, giving the ratio $S_k=n_{k+1}n_e/n_k=f(T)$, is valid in the range of temperatures and

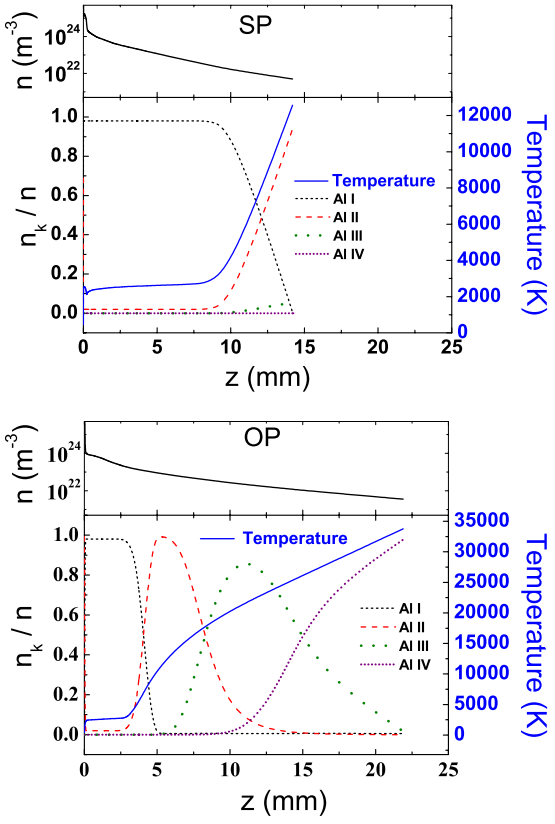

FIG. 4. (Color online) Spatial profiles of atomized species (neutral+ions) density $n(z)$, temperature $T(z)$, and species proportions n_k/n of atoms Al-I to Al-IV. The profiles are simulated for a time $t=250$ ns after the laser impact in case of SP and OP laser intensity distributions. The location $z=0$ corresponds to the initial metal surface. The incident fluence is 5.8 J/cm^2.

densities of interest in this work, it can be used to express n_1 (density of ionized one time atoms Al-II) as a function of n_e and S_k,

$$n_1 = \frac{n_e}{1 + \sum_{k=2}^{k_{\max}} k \frac{\prod_{l=1}^{k-1} S_l}{n_e^{k-1}}}. \quad (5)$$

Densities n_2 to n_{13} of Al-III to Al-XIV are computed recursively with Saha ratio S_k and the density n_0 of neutral atoms Al-I is given by $n_0 = n - \Sigma_{k=1}^{k_{\max}} n_k$. Figure 4 shows spatial profiles of atomized species (neutral+ions) density $n(z)$ and temperature $T(z)$. The species proportions n_k/n of atoms Al-I to Al-IV are computed at 250 ns after the moment of energy deposition (corresponding to the middle of experimental acquisition time gate) with femtosecond SP and temporally optimized OP laser pulses. In the following, the areas occupied by the different species are determined using the FWHM of the axial distributions. Several observations can be made. The maximum distance from the surface achieved by the front of the simulated plasma plume at 250 ns is higher with the optimized pulse OP (about 22 mm) than with SP (about 14 mm). The analysis of the spatial profiles of atoms in different ionization stage ratio (n_k/n in Fig. 4) reveals that those species tend to agglomerate in spatially distinct locations. This will be discussed in the following section. Close to the surface, the proportion of ionized atoms is low and the plasma consists mainly of Al-I. The temperature spatial profile *in the vicinity* of the surface is almost constant (~2600 K) independent of the temporal pulse shape. However, the length of the area occupied by neutral atoms and the ionization state (and temperature) of the simulated plume front are strongly influenced by the temporal tailoring of incident energy. The femtosecond SP induces a low excitation plasma configuration with a large area dominated by neutral atoms (12.5 mm) and a temperature of 12 500 K at the front mainly occupied by Al-II ions. Comparatively, the optimized pulse OP leads to a plasma of higher excitation state with a smaller area associated with Al-I (0–4 mm) and a high front temperature (34 000 K) producing a majority of Al-IV (not measured). Al-II atoms are concentrated at the front of the plume for the femtosecond SP while they are localized closer to the solid surface when OP is applied (between 4 and 8.5 mm). The size of Al-II area is larger with OP (4.5 mm) than with SP (1.5 mm) and the density state corresponding to each area is more than one order of magnitude higher for OP (from 4×10^{22} to 10^{23} m^{-3}) than for SP (6×10^{21}–9×10^{21} m^{-3}), as shown in Fig. 4.

Although experiment and simulation reveal a good qualitative agreement, several discrepancies between experimental and numerical results are observed, in particular, concerning the temperature values of the ionic species. Two main elements can be invoked to explain these differences. First, experimental observations are integrated over the range 100–400 ns, this being a temporal window during which the plasma has a fast dynamics and cools down. As well, the spectral emission measurement is spatially averaged, detecting simultaneously species located at different regions. Second, the numerical simulations are based on one-dimensional calculation as explained in the previous section. Nevertheless, we can reasonably suppose that our approach remains acceptable to give a qualitative picture of the plume behavior, including the spatially distinct aglomeration of species following the temperature profile and its maximum at the plasma front.

C. Discussion

The comparison between the experimental and numerical results presented above allows to address several interpretation questions concerning the laser-induced ablation and plume expansion processes. As reported in Sec. IV A, the estimated excitation temperatures of Al-I and Al-II are found to be different. Although difficult to be resolved due to the spatial integration of spectroscopic measurements along an inhomogeneous plasma,[81] this could be correlated with potential generation of different agglomeration zones for those species as recently reported in Ref. 82. Although several mechanisms can be involved, this is consistent with the simulation results presented above which indicate that the spatial temperature and density profiles of the ablation plume are not constant along the expansion axis[83] and induce spa-

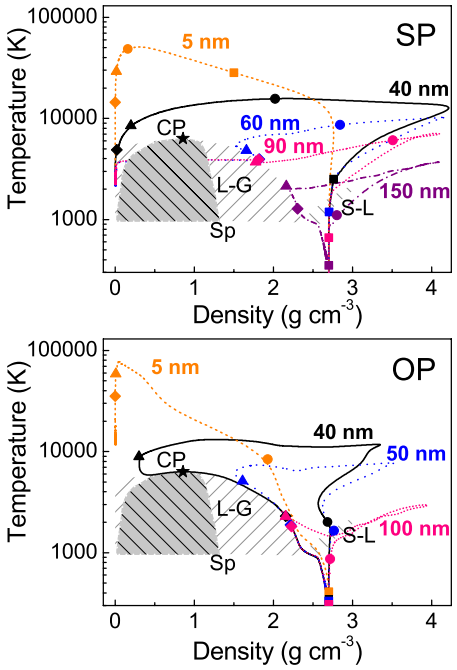

FIG. 5. (Color online) Thermodynamic trajectories of several simulation cells within the excited aluminum region in a density-temperature (ρ-T) diagram for a short and optimized laser pulse (SP and OP). The cells correspond to material layers initially situated at different depths. Different relevant moments with respect to the beginning of the laser exposure: 1 ps, 10 ps, 100 ps, and 1 ns, are, respectively, marked by square, circle, up triangle, and diamond symbols. The simulation ends at 250 ns. The incident fluence value is 5.8 J/cm^2 (more than one order of magnitude above the ablation threshold). The solid-liquid (S-L; melting), the liquid-gas (L-G; binodal), and the onset of instabilities (Sp; spinodal) boundaries given by the EOS, as well as the position of the critical point (CP) are also depicted on the figure. Due to the uncertainty related to the passage via the instability region, the thermodynamic trajectories are not shown below the spinodal envelope.

tially distinct locations of atoms in different ionization stages as suggested by the Saha law. This is a notable observation since the model used in our simulation does not take into account gas-phase charge interaction and inherent internal electric fields in the plume. This may lead to further charge separation[84] preserving however the species sequential distribution.

With the two temporal distributions of laser energy tested here, the irradiation leads to a plasma plume characterized by a decreasing density and a two-step behavior for the temperature with the distance from the solid surface. The temperature profile is quasiconstant close to the surface and increases until the maximum value obtained at the front of the plume. This implies that at least two different mechanisms are involved in the plasma formation. To address this question, the numerical simulation is used to compute the thermodynamics paths followed by the material at different depths starting from the laser energy deposition up to 250 ns of evolution.

Figure 5 shows the results of the modeling applied to short and optimized pulses. These simulated thermodynamics paths indicate at least three remarkable types of behavior. In both cases, the superficial layers (from the initial surface to 40 nm deep) undergo a fast heating which leads to an expansion above the critical point (CP). As discussed previously in Ref. 6, that kind of high-temperature relaxation path corresponds to an excess of energy which offsets the intermolecular potentials leading to a reduction in the latent heat of vaporization. The energy of atoms in the condensed phase becomes comparable to their binding energy inducing the decomposition of the hot fluid in gas-phase atomic species without involving nucleation. This can be described by a fragmentation mechanism of the supercritical fluid in expansion and direct transition to plasma.[3,4] The atomization delivers hence the hot gaseous ejecta. The behavior of the initially 5-nm-deep layer allows the comparison between the laser-induced fragmentation with SP and OP. The maximum temperature achieved by this layer is larger with OP (77 500 K) than with SP (51 500 K). Moreover, the maximum specific energy stored in this layer is twice larger with OP (1.68×10^8 J/Kg) than with SP (5.71×10^7 J/Kg). We can conclude that the atomization of the hot fluid process is induced at a higher temperature and specific energy for OP than for SP taking a favorable turn. As a side note, the layer corresponding to the cell located initially at a depth of 40 nm follows a supercritical expansion path in the OP case and then recondenses. This behavior can be attributed to the excess of specific energy stored in the upper layers which induces additional compression of this particular layer. The second type of behavior is related to deeper layers undergoing a moderate heating accompanied by a strong compression. This leads to an expansion path under the critical point which crosses the binodal line and reaches the gaseous state. This corresponds to the rapid homogenous nucleation of gas in the metastable liquid and determines the ejection of a liquid-gas mixture.[68] The associated ablation process can be accounted for with the so-called phase explosion mechanism.[3,8,85] The deepest layers simulated here undergo the last type of behavior: a low heating accompanied by a strong compression. During the following relaxation, these layers expand and reach the limit of coexistence between liquid and gas before recondensing along that binodal line.

Referring to the last two evolutions, results presented in Fig. 5 shows that layers initially located between 60 and 90 nm in the SP exposure and between 50 and 100 nm for OP case behave differently. In the OP case, the compression is reduced and the layers recondense without crossing the binodal limit. With the SP irradiation, the layers initially located at depths between 60 and 90 nm undergo a strong compression of the matter followed finally by a phase-explosion-like mechanism (nucleation-based) as they enter in the metastable region. However due to particularly strong mechanical load associated with SP some confinement effects occur.[6] In their evolution part of these layers follow the binodal limit during a long time (nanosecond time scale) before crossing it (note the corresponding moments indicated in Fig. 5). This behavior corresponds to the ejection of liquid droplets and will be discussed in more details in the last section. This comparison between the behaviors of deeper layers with SP and OP irradiation indicates a reduction in the phase explosion efficiency and an increase in recast when using the optimized laser energy distribution. We recall here the additional heating of the superficial layers with OP.

By comparing these results with the different temperature and density spatial profiles presented in Fig. 4, we can conclude that a consistent part of the plasma formed by neutral species at quasiconstant lower axial temperature and located close to the solid surface is generated by the rapid homogenous nucleation of gas in the metastable liquid. This typically leads to the ejection of a liquid-gas mixture. The leading part of the ablation plume with increasing temperature along the axis is induced by the atomization of the supercritical fluid which produces hot gaseous ejecta. The initial absorption profile during energy deposition is responsible for this increasing temperature profile observed at 250 ns. It is particularly the relative weight of the thermodynamical paths that is affected by the temporal distribution of the incoming energy.

The different behaviors generated by SP and OP sequences can be discussed on the basis of the initial arguments presented in Ref. 6 which shows that the thermodynamic states variations during the laser ablation can induce an enhanced energy coupling in the material. This is correlated with electronic collisional effects and density changes according to the phase transformation succession.[86] While in case of SP, the materials stays mainly in condensed phase with optical properties determined primarily by temperature (and therefore fluence)-induced collisional effects and vary little during the melting phase,[87] these optical properties are transiently modified during the optimized irradiation sequence as density varies. This behavior is superposed initially on pure temperature-induced collisional effects and takes over during the sequence via an intricate mixing of temperature and density variations. As a proof, specific examples of transient reflectivity behaviors are shown in Fig. 6 for particular shapes and will be discussed in the next paragraphs. We note for the moment the drop of reflectivity associated with the onset of hydrodynamic advance (arrow mark) for the shaped pulses preceded by a temperature effect (enhanced for SP and high intensities).

This allows to adapt the incoming energy rate to enhance the absorption, resulting in the augmentation of the heat load in the superficial layers in the case of OP irradiation. This hypothesis is supported by the previous analysis of thermodynamic paths of those layers (presented in Fig. 5) associated with higher maximum temperature and specific energy generated with OP than with SP. We conclude that the onset of hydrodynamics effects during the OP exposure (going up to plasma ignition), such as expansion and the consequent drop of reflectivity of the irradiated surface, allows an enhancement of the energy deposition in the first material layers due to the variation of the optical and transport properties. This will be experimentally confirmed in the following section. Finally, these results allow to indicate that in our high fluence conditions, the optimization does not lead to a luminescence increase but induces a higher ionization state in the plasma plume.

In this context, the enhancement of the ionic signal with respect to the neutral emission with the optimized pulse OP is achieved through the more efficient channeling of the incident energy into the superficial layer. This enhances the efficiency of the atomization of the supercritical fluid with respect to nucleation-based mechanisms. Moreover, the optimized pulse generates an Al-II dominated area at higher densities with respect to the SP-induced configuration (as reported in Fig. 4). Consequently, the optimized laser energy distribution enhances the number of Al-II and reduces the one of Al-I. We thus suppose that the plasma emission optimization with respect to the excitation degree is strongly related to the evolution of the emitter's quantity of the different species. The ionization degree is augmented without changing the total energy of laser pulses. The optimized temporal tailoring of the laser exposure sequence allows therefore to redistribute and increase the excitation of the plasma plume with a reduced energy cost through a more synergetic interaction with the irradiated material. This appears to be intrinsically related to provoking and making use of a reflectivity drop along side with density variations impeding thermal transport.

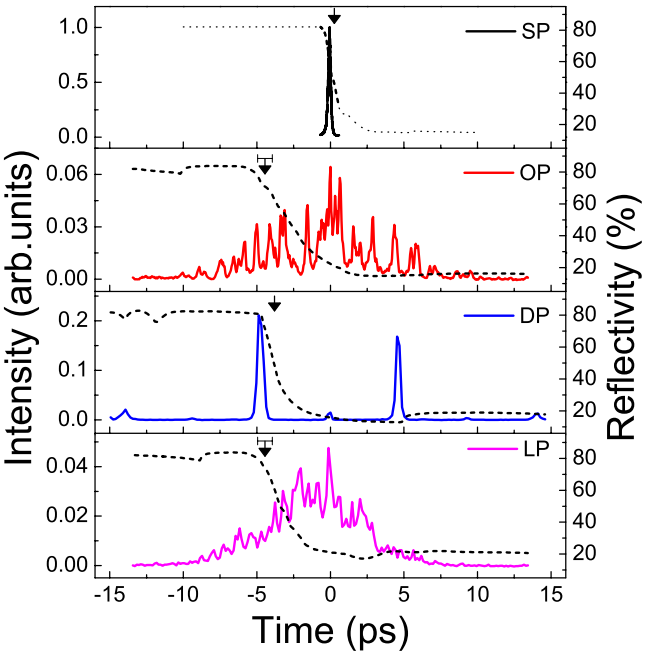

FIG. 6. (Color online) Temporal distribution of the intensity (solid lines) for the short pulse (SP), the optimized pulse (OP), the double pulse (DP) with 10 ps delay and the long pulse (LP) of 6 ps FWHM duration determined by cross-correlation methods. Corresponding calculated transient reflectivities of the excited sample (dashed lines). The dotted line in the SP case is a guide for the eyes. The arrows indicate the observable expansion onset for the simulated layer initially located at 10 nm deep.

The shape of the laser pulse can create a complex topology of the interaction space. In order to simplify and understand its influence on the interaction process, we employ designed pulses which gather features of the OP: two short peaks (250 fs duration) with a separation delay of 10 ps (DP) and a Gaussian stretched pulse (LP) of 6 ps FWHM. This was achieved by applying cyclic rectangular π-phase profiles or parabolic phase masks on the SLM. Figure 6 shows intensity cross-correlation traces together with a sketch of reflectivity behavior for the excited matter in each case calculated as indicated in Ref. 72, taking into account the effect of time-evolving collision frequency and the dynamic variation in density and temperature. The arrows indicate the moments

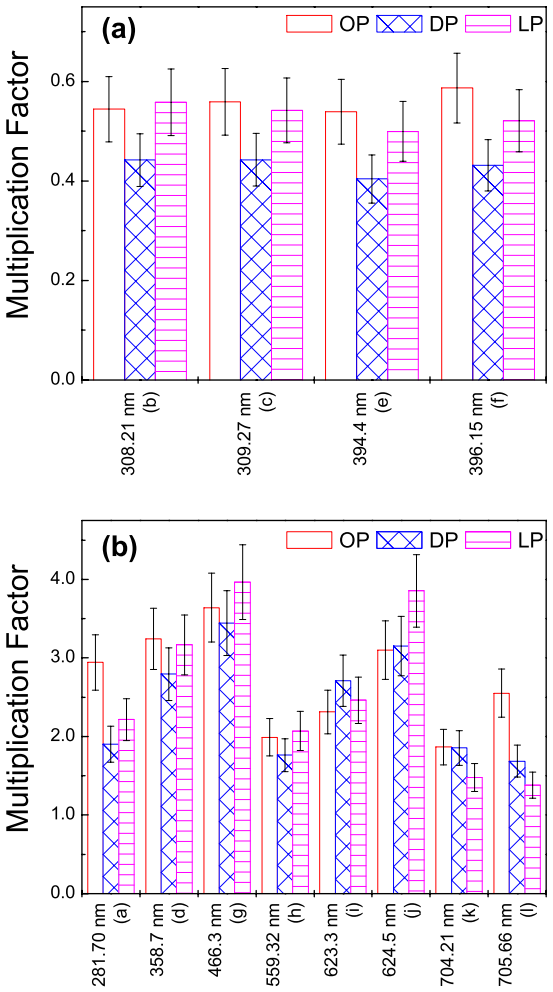

FIG. 7. (Color online) Evolution of the (a) neutral and (b) ionic lines emission in the UV-VIS domain with optimized OP, long LP, and double DP pulses at 5.8 J/cm^2 (the multiplication factor is given with respect to the lines intensities generated by the short pulse SP). The letters in the brackets indicate the line assignment corresponding to Table I.

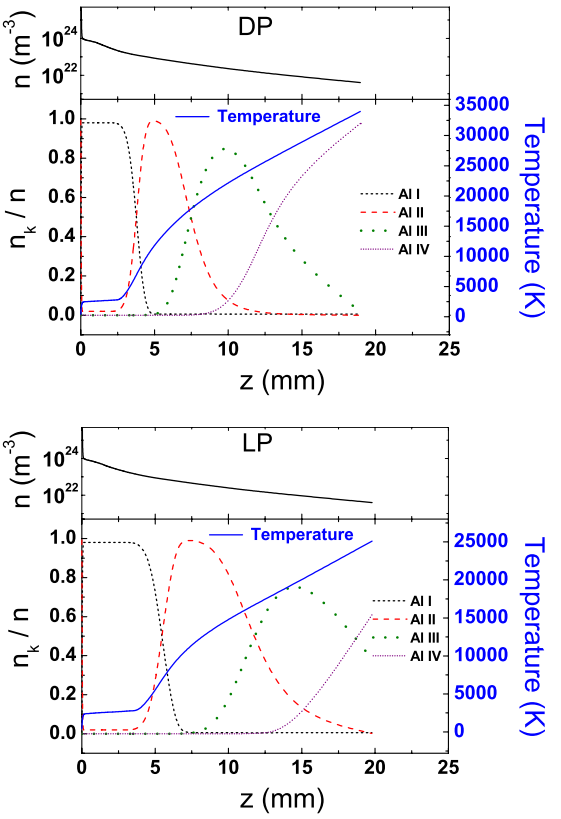

FIG. 8. (Color online) Spatial profiles of density $n(z)$, temperature $T(z)$, and species proportions n_k/n of atoms Al-I to Al-IV simulated at t=250 ns after the laser impact for temporally tailored incident DP and LP (z=0 at the surface). The incident fluence is 5.8 J/cm^2.

of the observable expansion onset for the simulated layer initially located at 10 nm (corresponding approximately to the optical penetration depth). This criterion gives an imprecision ranging from few tens of femtosecond for the SP exposure up to one picosecond in the case of stretched energy depositions. For all shaped pulses, the drop in reflectivity and the subsequent augmentation of the absorbed energy allow already to anticipate the possibility of a modified plume behavior. The influence of irradiation coupled via a change in transient optical properties as the hydrodynamic movement commences was indicated in Ref. 6 and we note here a particularly strong effect on the plume. The emission lines reported in Table I induced by DP and LP are investigated and compared with OP and SP results. A summary of the multiplication factors associated with each spectroscopic line in these three configurations of energy deposition is given in Fig. 7. As already observed with OP, the distributions DP and LP induce a reduction in neutral lines intensity [(e) and (f) in Table I] and an enhancement of ionic lines (d) emission. The intensity of the ionic line (d) is multiplied by 2.8 for DP and 3.2 for LP (with respect to short pulse irradiation), while neutral transition [(e) and (f)] intensity are, respectively, divided by 2.5 and 2.3 for DP and by 2 and 1.9 for LP. Intensity integrated for all neutral lines in our detection range is reduced in both cases ($M_{\mathrm{DP}}^{\mathrm{Al\text{-}I}}=0.43\pm0.05$ and $M_{\mathrm{LP}}^{\mathrm{Al\text{-}I}}=0.52\pm0.06$) while the sum of ionic transitions intensity is multiplied by 2.8 for DP and 3 for LP. Total transition intensity is also reduced (divided by 1.6 for DP and 1.4 for LP). With DP (respectively, LP), 62% (65%) of this total intensity is emitted by Al-I and 38% (35%) by Al-II.

Experimentally determined averaged excitation temperatures induced by DP and LP are, respectively, $T_{\mathrm{DP}}^{\mathrm{Al\text{-}I}}=5600\pm400$ K, $T_{\mathrm{LP}}^{\mathrm{Al\text{-}I}}=5600\pm400$ K for Al-I and $T_{\mathrm{DP}}^{\mathrm{Al\text{-}II}}=24\,000\pm2000$ K and $T_{\mathrm{LP}}^{\mathrm{Al\text{-}II}}=19\,000\pm2000$ K for Al-II. Experimental ablation rates are reduced with respect to the SP case and close to the one generated by OP (respectively, 79 ± 4 nm/pulse for DP and 83 ± 4 nm/pulse for LP).

We note that these behaviors are typical for a rather high fluence regime with respect to the threshold, namely, the ionization increase on the expense of neutral population. Complementary behaviors on overall yield increase at lower fluences were noted recently.[88] To emphasize the specific features in these conditions, the numerical simulation presented above is also applied to the double and stretched pulses DP and LP. Figure 8 shows the calculated spatial profiles of atomic density $n(z)$, temperature $T(z)$, and proportion

of Al-I to Al-IV density numbers at 250 ns after the laser impact. The maximum distance from the surface achieved by the simulated plasma with LP and DP are quite similar (respectively, 20 nm and 19 mm) and slightly lower than with OP. LP irradiation leads to a Al-I occupied area close to the surface (from 0 to 5.5 mm) larger than OP exposure. The smallest Al-I area is produced with DP (from 0 to 3.8 mm). The maximum calculated temperature (at the plasma front) obtained with LP (~24 000 K) is lower than with OP. The extension of the Al-II area (6 mm) produced with LP is slightly larger than with OP but is also associated with a lower density (from 1.6 to 7.7×10^{22} m^{-3} for LP and from 4×10^{22} to 10^{23} m^{-3} in the OP case). In the case of DP exposure, the maximum temperature achieved at the plasma front is similar to the one simulated for OP (~34 000 K). The Al-II area is associated with the same range of densities as with OP (4×10^{22} to 1×10^{23} m^{-3}) but its extension is reduced (3.7 mm). These numerical results seem consistent with the experimental emission intensity measurements presented in Fig. 7, indicating relatively small differences between the optical plasma emission induced with OP, DP, or LP with respect to Al-II versus Al-I intensity ratio enhancement.

D. Pre-excitement requirements for improved coupling

It was mentioned before that several different results of the optimization perform similarly with respect to the plasma emission. A first example was given above with a second optimization result leading to the optimal laser sequence OP′ depicted on Fig. 2(d). This section intends to propose a deeper perspective on the influence of the optimized pulse on the ablation process. From the analysis, it seems that a large class of laser-pulse temporal shapes allows to perform the optimization task and increase the plasma excitation with a high efficiency. These observations pertain also the designed pulses, the Al-II optical signal enhancement generated with OP′ being also similar to the one obtained with OP, DP, and LP. A common feature of the adapted laser sequences is the stretched energy deposition on several picosecond. This allows an optimal preparation of the irradiated material by the leading part of the pulse, an efficient absorption of the trailing part and, consequently, a maximization of the effect of plasma excitation. The questions that impose themselves concern the nature of this "preparation" and the related energetic requirements.

To elucidate which mechanisms have to be triggered during this preparation, we have designed the following experiment that temporally separates the preparation phase from the main absorption events. We use nonsymmetrical double pulses separated by 11 ps as depicted in Fig. 9(a) where the level of the leading peak was gradually increased while preserving constant the total energy. This was achieved using V-shaped spectral phase masks with variable cusp position. The plasma emission was monitored at the same time. This experimental approach allows to progressively enhance the energy involved in the preparation process by controlling the energy balance between the two peaks. We were concerned here with a brief evaluation on the picosecond-spaced

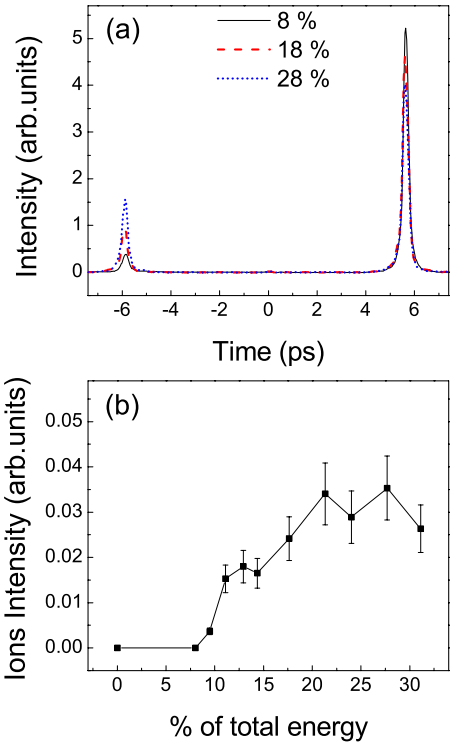

FIG. 9. (Color online) (a) Example of asymmetric double pulses (11 ps separation) with different energy balance between the two peaks at constant total energy. The energy contained in the leading peak is gradually increased to "prepare" the material for an enhancement of the energy coupling. (b) Al-II optical emission intensity evolution [line labeled (d)] with the double pulses energy balance (first peak contribution) at 1.1 J/cm^2.

prepulse forms leading to the onset on ion enhancement. To increase the sensitivity of the measurement we have chosen a lower fluence, slightly below the threshold of SP ion observation (1.1 J/cm^2). Although the succession of phenomena may be changed,[88] this was motivated by the fact that at the regular fluence of 5.8 J/cm^2 the effect was starting at prepulse intensities too low with respect to the main peak for permitting an accurate measurement. The procedure allows to detect and characterize the Al-II emission increase in the line labeled (d) in Table I with the augmentation of the energy consumed for the surface preparation (i.e., energy in the first peak). The results, shown in Fig. 9(b), indicate a threshold energy for the first peak (corresponding to 10% of the total energy) required to initiate the Al-II signal enhancement. This signal achieves a maximum for an energy balance of 25–75 %. Converting these percentages to fluences of the first peak indicates an ion signal rise at the fluence threshold of 0.1 J/cm^2 (close to the optical modification threshold) and a maximum increase achieved for 0.28 J/cm^2 (just below the onset of visible macroscopic ablation). These results suggest that the optimal preparation with respect to the plasma excitation enhancement is related to the onset of the hydrodynamic movement of the excited material induced by the leading part of the laser exposure. On the picosecond time scale, the material expansion is associated with a drop of the reflectivity as shown in Fig. 6 (however at a higher fluence). This leads to an enhanced coupling of the trailing

part of the laser pulse and consequently increases the absorbed energy per atoms. As final remark, we note that, as the geometry involves several passages over preirradiated target regions, the possible rippled structure at pulse overlapping complicates the accurate interpretation of the laser-matter interaction.

In summary, the optimized pulse favors a conversion of the laser incoming energy into thermal energy of the expanding material inducing a surface transformation mainly mediated by the atomization of the supercritical fluid. The energy is more efficiently channeled in the superficial layers and the ablation rate is reduced. This is also consistent with previous observations[6] indicating an effective mechanical to thermal energy conversion for longer pulse envelopes. The femtosecond pulse leads to a preferential channeling of the laser energy into a gas-phase transformation that proceeds dominantly in the metastable region via nucleation and induces a higher ablation rate. This indicates a possible adjustable balance between the amount of ejected gas-liquid mixture (subsequent to nucleation) and the excitation of the gaseous fraction of ablated matter (through the atomization of the supercritical fluid). Modifying the energetic state of the plasma plume may then influence PLD processes through the nanoparticles generation.

V. INFLUENCE ON NANOPARTICLES DEPOSITION

To study the effect of the temporal shape of various laser pulses on the collected material from the plume, thin films were elaborated by pulsed laser deposition with irradiation sequences provided by SP, OP, LP, and DP ($N=9\times10^5$ pulses, $P\sim10^{-5}$ Pa). The FEG-SEM images of the resulting films are presented in Fig. 10. The surface morphologies of the deposited films are dominated by nanoparticles (with radii between tens and hundreds of nanometer) with a density strongly dependent on the temporal profile of the laser pulses. Nanoparticles radius distributions, ranging from 30 to 200 nm and displayed in Fig. 11, indicate a decrease in the particles density from SP (presenting the highest number of nanoparticles) to DP film (density minimum). Intermediate distributions can be determined for OP- and LP-induced films. The relative abundance of each radius is displayed in double-logarithmic scale in the inset of Fig. 11 and is similar for the four temporal distributions. These size distributions $f(r)$ are characterized by a two slope behavior with $f_1(r)\sim r^{-2}$ for $r<80$ nm and $f_2(r)\sim r^{-3.7}$ for $r>80$ nm, which is in concordance with previous reports in the literature.[27]

Two main classes of processes are usually invoked to address the problem of nanoparticle generation[20]: condensation or nucleation of particles in the plasma or gas phase on one hand and direct ejection of aggregates from the liquefied target on the other hand. The condensation processes are dominant when the collision rate between particles in the atomic vapor is high with respect to the characteristic time of the expansion.[20] These mechanisms were found to lead to nanoparticles with low radii ranging from few nanometer to few tens of nanometers.[20,21,89,90] The direct liquid ejection mechanisms are associated to the formation, hydrodynamic motion, and ejection of liquid-density layers separated by lower-density gaps composed by a liquid-gas mixture[6,20,19,91–93]. This structuring of the ablated matter is a consequence of the rarefaction waves propagation in the irradiated material during the first stages of expansion.[94,95] The above observations suggest that this mechanism can be controlled by the balance between mechanical and thermal energies of the expanding material.[96] Influences are expected as well on the condensation mechanism as temperature and pressure condition may vary.

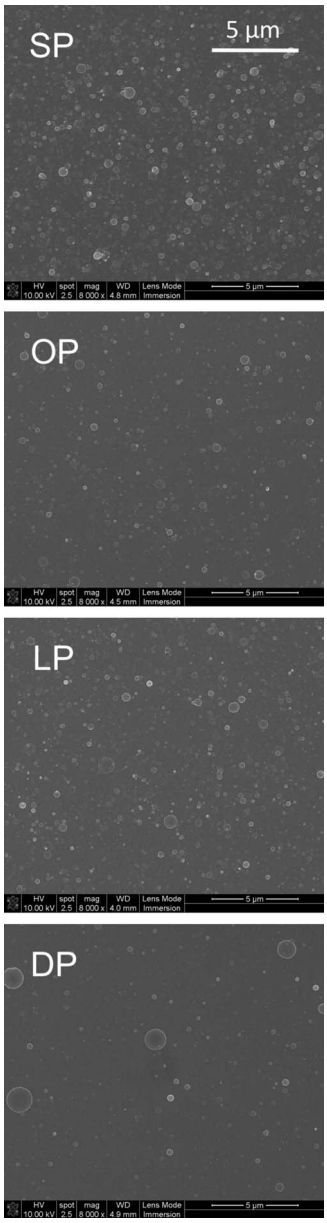

FIG. 10. SEM images of thin films produced with SP, OP, LP, and DP indicating the presence of nanoparticles in different contents and sizes.

We will focus below on the second mechanism (direct ejection of liquid particles) to explain our experimental findings, especially for larger size particulates. The reduction in nanoparticles deposition on the film surfaces seen in Fig. 11 can be linked to the enhancement of plasma excitation via a temperature control mechanism as this may influence the

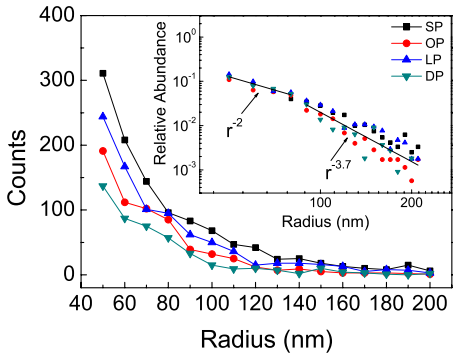

FIG. 11. (Color online) Nanoparticles radius distributions on the surfaces of films produced with SP (square), OP (circle), LP (upward triangle), and DP (inward triangle). Inset: normalized particles abundance with respect to radii for SP, OP, LP, and DP (double-logarithmic scale) and fit lines in the form of r^{α} with $\alpha=-2$ for $r<80$ nm and -3.7 for $r>80$ nm.

thermomechanical balance. At the fluence used here (5.8 J/cm^2), the plasma heating is associated with the increase in the ionic signal in this case on the expenses of neutral population. These aspects were previously identified to be the consequence of reaching supercritical fluid states rather than entering the two-phase region as noted for SP. This shows a strong correlation between the nanoparticles generation and the mechanisms leading to a gas-liquid mixture ejection directly from the target to which we add the distinct mechanical ejection of liquid layers. These liquid layers were indicated in hydrodynamic simulations as long-living along binodal liquid-density plateaus sandwiched between gas layers upon expansion.[6,20] Inhomogeneous matter expulsion was also confirmed by the time-resolved optical microscopy observations reported in Ref. 94.

We will follow below the evolution of the nanolayers that have consequences on nanoparticles accumulation on substrates in different conditions of exposure feedthrough. As exposed in Refs. 20 and 93, the ablated matter configuration discussed above can lead to a direct mechanism of nanoparticles generation. If the plateau lifetime is long enough, a Rayleigh-Taylor instability can occur inducing the decomposition of the liquid layer in droplets with radii described by[20,93]

$$r_p = \left(\frac{9\pi h_p^2 \sigma}{P_i}\right)^{1/3}, \tag{6}$$

where h_p is the thickness of the plateau, σ the surface tension, and P_i the pressure between the gap and the plateau. Droplets can also be formed in the gap through the competitive actions of hydrodynamics and surface-tension forces. The maximum radius of stable droplets is then given by[20,93]

$$r_g = \left[\frac{15\sigma}{\rho(dv/dz)^2}\right]^{1/3}, \tag{7}$$

where ρ is the density and dv/dz is the velocity gradient in the gap.

To address more precisely the contribution of the liquid layer ejection and decomposition through Rayleigh-Taylor instabilities to the nanoparticles generation in our case, the results of the hydrodynamic simulations described above are used to compute the material density profile $\rho(z)$ close to the solid surface at different moments after the laser impact (500 ps, 1, 5, and 10 ns) for the four temporal distributions of energy deposition (SP, OP, DP, and LP). The results are reported in Fig. 12. The position $z=0$ corresponds to the solid

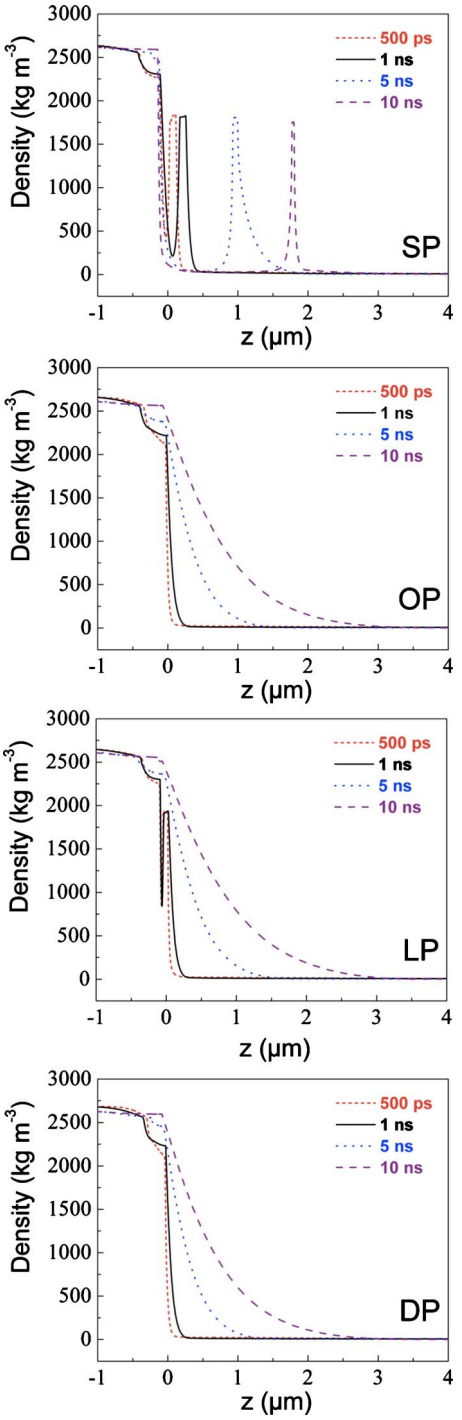

FIG. 12. (Color online) Density profiles at four different moments during the simulated hydrodynamic expansion of Al under the action of SP, OP, LP, and DP laser pulses. The observed plateau at quasiliquid density corresponds to a confined liquid phase. The incident fluence is 5.8 J/cm^2.

surface (bulk for $z<0$). The profile induced with the SP at 500 ps shows a plateau at liquid density separated from the surface by a thin gaseous area. This plateau survives until 10 ns and is moving away of the surface (at ~ 200 m/s). The temporal distribution LP generates a plateau resembling pattern, with less distinct separation from the unablated matter. The latter is suppressed after several nanosecond and recondensation at solid density occurs. The OP and DP exposures do not lead to the formation of a plateau at liquid density, we only observe a continuous decreasing from solid to low density.

Moreover, the simulation results can be used to calculate the droplets radii described by the Eqs. (6) and (7). In our conditions, the lifetime of the quasiliquid-density plateau can be estimated between 1 and 10 ns. Then we choose to evaluate the droplets sizes associated to the ejection and decomposition of the plateau in the case of SP irradiation sequence at $t=10$ ns after laser exposure. The numerical computation results allows to estimate the different parameters involved: the plateau thickness $h_p=25$ nm, the pressure between the gap and the plateau $P_i=3.13$ MPa and the velocity gradient in the gap $(dv/dz)=1.6\times 10^9$ s^{-1}. The density of liquid aluminum is taken as $\rho=2500$ kg m^{-3}. The surface tension is calculated through the following equation[97] $\sigma=\sigma_0+a(T-T_m)$ with $\sigma_0=0.83$ Nm^{-1} the surface tension of the equilibrium liquid, $a=-1.34\times 10^{-4}$ N m^{-1} K^{-1} a phenomenological constant and T_m the melting temperature of Al. The simulated temperatures in the plateau and in the gap at 10 ns after laser irradiation are 3900 K and 3800 K, respectively. We obtain liquid surface tensions of 0.46 Nm^{-1} in the plateau and 0.47 Nm^{-1} in the gap that intervene in estimating the radii. The mean radius of droplets formed consequently to the plateau decomposition is $r_p \approx 140$ nm while the maximum radius of particulates formed in the gap is $r_g \approx 100$ nm. These values are in good agreement with the experimental findings presented in Fig. 11, being at the middle of the distributions.

Several effects induced by the temporal shaping of laser pulses with the optimal sequences (OP, LP, and DP) can be now correlated. The experimentally observed nanoparticles density is reduced without a change in the relative abundance. The phase explosion efficiency is progressively decreased in the favor of hot material decomposition that accentuates the efficiency of the transition to gas phase. The computed evolving liquid-density plateau is progressively suppressed. These observations suggest that the decomposition following the instability of the ejected liquid shell plays a major role in the formation of nanoparticles of radii <200 nm induced by femtosecond laser ablation in our energetic conditions.

VI. CONCLUSION

In conclusion, we have shown the possibility to influence and optimize the optical emission of the different atomic species in the ablation plume from ultrafast laser irradiated Al targets. An adaptive procedure based on the spectroscopic analysis of the plasma luminescence was used to lock up the temporal shapes for laser pulses which determine specific emission signals of the plume. The enhancement of the ionic (Al-II) emission with respect to the neutral (Al-I) signal is achieved through a suited temporal tailoring of the laser pulses on picosecond scales. The influence of this optimized temporal distribution on optical plasma emission is compared to simpler shapes corresponding to stretched and double pulses in order to provide insights into the optimization processes. While the femtosecond unshaped pulse leads to a weak ionization level, the optimized, double, and long pulses (LPs) generate a larger amount of Al-II ions in the leading part of the plume following a strong temperature gradient at the front. Consequence of a higher and more confined energy coupling, this is achieved through an optimal surface pre-excitation by the leading part of the laser pulse which enhances the absorption of the trailing part. The energy threshold to establish an efficient preparation of the superficial layers is determined. The optimization effect starts with the onset of optical modification and is maximum close to the visible macroscopic ablation threshold. As the energy is coupled in the evolving material, this leads as a side consequence to a lower ablation rates for the temporally shaped pulses than those induced by the femtosecond pulse.

Thin films were elaborated in order to study the influence of temporal shaping of laser pulses on the PLD processes. The efficiency of nanoparticles generation appears to be also controllable through the temporal shapes of the laser pulses. The femtosecond unshaped pulses leads to a high density of nanoparticles at the deposition surface. The use of the optimized, double, or stretched pulses allows to reduce the nanoparticles production by balancing the thermomechanical energy content.

Numerical simulations were performed to support the interpretation. The theoretical results allow to explain the influence of the laser pulses temporal shape on optical plasma emission in terms of modifications of the spatial temperature and density profiles in the plasma. Moreover, the efficiency of the nanoparticles generation can be correlated with the ejection of nanosized liquid layers. This liquid layer could lead to nanoparticules formation through its decomposition following a Rayleigh-Taylor instability or surface-tension phenomena.

The reported influence of the temporal shaping of femtosecond laser pulses on the optical plasma emission and on nanoparticles generation implies a direct modification of the ablation mechanisms. Our study suggests that the temporal shaping of initially ultrafast laser pulses allows to control the balance between the different relaxation paths of the incident energy. In particular, the femtosecond laser pulse induces an ablation dominated by homogeneous nucleation processes in the liquid phase. The optimal tailoring of the laser pulses allows to reduce the weight of the phase explosion process and to enhance the mechanisms related to the atomization of the supercritical fluid inducing a more efficient transition to the gas phase. Through the temporal pulse shape the balance between the two mechanisms can be regulated.

The influence, reported in this paper, of the femtosecond laser pulses temporal tailoring on the relaxation paths followed by the excited matter opens a range of perspectives, in particular, in the field of PLD or LIBS applications where the control of ablated materials characteristics is of prime interest.

ACKNOWLEDGMENTS

The authors would like to thank Patrick Combis from Commissariat à 1'Énergie Atomique (CEA) for his support in the development of the Esther code provided by CEA and acknowledge the generous support of the Agence Nationale de la Recherche.

*florence.garrelie@univ-st-etienne.fr
†razvan.stoian@univ-st-etienne.fr

[1] B. N. Chichkov, C. Momma, S. Nolte, F. von Alvensleben, and A. Tünnermann, Appl. Phys. A: Mater. Sci. Process. **63**, 109 (1996).
[2] R. Le Harzic, N. Huot, E. Audouard, C. Jonin, P. Laporte, S. Valette, A. Fraczkiewicz, and R. R. Fortunier, Appl. Phys. Lett. **80**, 3886 (2002).
[3] D. Perez and L. J. Lewis, Phys. Rev. B **67**, 184102 (2003).
[4] J. P. Colombier, P. Combis, F. Bonneau, R. Le Harzic, and E. Audouard, Phys. Rev. B **71**, 165406 (2005).
[5] F. Vidal, T. W. Johnston, S. Laville, O. Barthélemy, M. Chaker, B. Le Drogoff, J. Margot, and M. Sabsabi, Phys. Rev. Lett. **86**, 2573 (2001).
[6] J. P. Colombier, P. Combis, A. Rosenfeld, I. V. Hertel, E. Audouard, and R. Stoian, Phys. Rev. B **74**, 224106 (2006).
[7] M. E. Povarnitsyn, T. E. Itina, M. Sentis, K. V. Khishchenko, and P. R. Levashov, Phys. Rev. B **75**, 235414 (2007).
[8] A. K. Upadhyay, N. A. Inogamov, B. Rethfeld, and H. M. Urbassek, Phys. Rev. B **78**, 045437 (2008).
[9] D. P. Banks, C. Grivas, J. D. Mills, R. W. Eason, and I. Zergioti, Appl. Phys. Lett. **89**, 193107 (2006).
[10] R. Fardel, M. Nagel, F. Nüeschb, T. Lippert, and A. Wokaun, Appl. Phys. Lett. **91**, 061103 (2007).
[11] B. Le Drogoff, J. Margot, M. Chaker, M. Sabsabi, O. Barthélemy, T. W. Johnston, S. Laville, F. Vidal, and Y. von Kaenel, Spectrochim. Acta, Part B **56**, 987 (2001).
[12] A. Assion, M. Wollenhaupt, L. Haag, F. Mayorov, C. Sarpe-Tudoran, M. Winter, U. Kutschera, and T. Baumert, Appl. Phys. B: Lasers Opt. **77**, 391 (2003).
[13] K. Stelmaszczyk, P. Rohwetter, G. Méjean, J. Yu, E. Salmon, J. Kasparian, R. Ackermann, J.-P. Wolf, and L. Wöste, Appl. Phys. Lett. **85**, 3977 (2004).
[14] J. Perrière, E. Millon, W. Seiler, C. Boulmer-Leborgne, V. Craciun, O. Albert, J. C. Loulergue, and J. Etchepare, J. Appl. Phys. **91**, 690 (2002).
[15] F. Garrelie, A. S. Loir, C. Donnet, F. Rogemond, R. Le Harzic, M. Belin, E. Audouard, and P. Laporte, Surf. Coat. Technol. **163-164**, 306 (2003).
[16] R. Teghil, L. D'Alessio, A. De Bonis, D. Ferro, A. Galasso, G. Lanza, A. Santagata, P. Villani, and D. J. Sordelet, Thin Solid Films **517**, 1880 (2009).
[17] M. Jelinek, A. Klini, C. Grivas, J. Lancok, V. Studnicka, J. Chval, A. Mackova, and C. Fotakis, Appl. Surf. Sci. **197-198**, 416 (2002).
[18] S. Eliezer, N. Eliaz, E. Grossman, D. Fisher, I. Gouzman, Z. Henis, S. Pecker, Y. Horovitz, M. Fraenkel, S. Maman, and Y. Lereah, Phys. Rev. B **69**, 144119 (2004).
[19] S. Amoruso, G. Ausanio, R. Bruzzese, M. Vitiello, and X. Wang, Phys. Rev. B **71**, 033406 (2005).
[20] E. Lescoute, L. Hallo, D. Hebert, B. Chimier, B. Etchessahar, V. T. Tikhonchuk, J.-M. Chevalier, and P. Combis, Phys. Plasmas **15**, 063507 (2008).
[21] T. E. Itina, K. Gouriet, L. V. Zhigilei, S. Noël, J. Hermann, and M. Sentis, Appl. Surf. Sci. **253**, 7656 (2007).
[22] S. Amoruso, R. Bruzzese, N. Spinelli, R. Velotta, M. Vitiello, X. Wang, G. Ausanio, V. Iannotti, and L. Lanotte, Appl. Phys. Lett. **84**, 4502 (2004).
[23] F. Garrelie, N. Benchikh, C. Donnet, R. Y. Fillit, J. N. Rouzaud, J. Y. Laval, and A. Pailleret, Appl. Phys. A: Mater. Sci. Process. **90**, 211 (2007).
[24] B. Liu, Z. Hu, Y. Che, Y. Chen, and X. Pan, Appl. Phys. Lett. **90**, 044103 (2007).
[25] J. Perrière, C. Boulmer-Leborgne, R. Benzerga, and S. Tricot, J. Phys. D **40**, 7069 (2007).
[26] S. Amoruso, R. Bruzzese, X. Wang, N. N. Nedialkov, and P. A. Atanasov, Nanotechnology **18**, 145612 (2007).
[27] S. Noël, J. Hermann, and T. Itina, Appl. Surf. Sci. **253**, 6310 (2007).
[28] M. S. B. Darby, T. C. May-Smith, R. W. Eason, T. Donnelly, J. G. Lunney, and K. D. Rogers, Appl. Surf. Sci. **254**, 3364 (2008).
[29] B. Sallé, O. Gobert, P. Meynadier, M. Perdrix, G. Petite, and A. Semerok, Appl. Phys. A: Mater. Sci. Process. **69**, S381 (1999).
[30] A. Semerok and C. Dutouquet, Thin Solid Films **453-454**, 501 (2004).
[31] R. Le Harzic, D. Breitling, M. Weikert, S. Sommer, C. Föhl, S. Valette, C. Donnet, E. Audouard, and F. Dausinger, Appl. Surf. Sci. **249**, 322 (2005).
[32] N. Jegenyes, J. Etchepare, B. Reynier, D. Scuderi, A. Dos-Santos, and Z. Tóth, Appl. Phys. A: Mater. Sci. Process. **91**, 385 (2008).
[33] S. Singha, Z. Hu, and R. J. Gordon, J. Appl. Phys. **104**, 113520 (2008).
[34] J. Alcántara, J. Vadillo, and J. Laserna, Appl. Phys. A: Mater. Sci. Process. **92**, 963 (2008).
[35] T. Donnelly, J. G. Lunney, S. Amoruso, R. Bruzzese, X. Wang, and X. Ni, J. Appl. Phys. **106**, 013304 (2009).
[36] I. H. Chowdhury, X. Xu, and A. M. Weiner, Appl. Phys. Lett. **86**, 151110 (2005).
[37] Y. P. Deng, X. H. Xie, H. Xiong, Y. X. Leng, C. F. Cheng, H. H. Lu, R. X. Li, and Z. Z. Xu, Opt. Express **13**, 3096 (2005).
[38] T. Y. Choi, D. J. Hwang, and C. P. Grigoropoulos, Appl. Surf. Sci. **197-198**, 720 (2002).
[39] Z. Zhang, P. A. Van Rompay, and P. P. Pronko, Appl. Phys. Lett. **83**, 431 (2003).
[40] R. Noll, R. Sattmann, V. Sturm, and S. Winkelmann, J. Anal. At. Spectrom. **19**, 419 (2004).
[41] V. I. Babushok, F. C. DeLucia, Jr., J. L. Gottfried, C. A. Munson, and A. W. Miziolek, Spectrochim. Acta, Part B **61**, 999 (2006).
[42] A. Santagata, R. Teghil, G. Albano, D. Spera, P. Villani, A. De Bonis, G. P. Parisi, and A. Galasso, Appl. Surf. Sci. **254**, 863 (2007).
[43] V. N. Rai, F. Y. Yueh, and J. P. Singh, Appl. Opt. **47**, G21

(2008).
[44] V. Pinon, C. Fotakis, G. Nicolas, and D. Anglos, Spectrochim. Acta, Part B **63**, 1006 (2008).
[45] R. Teghil, L. D'Alessio, A. Santagata, M. Zaccagnino, D. Ferro, and D. J. Sordelet, Appl. Surf. Sci. **210**, 307 (2003).
[46] N. Jegenyes, Z. Toth, B. Hopp, J. Klebniczki, Z. Bor, and C. Fotakis, Appl. Surf. Sci. **252**, 4667 (2006).
[47] S. Noël and J. Hermann, Appl. Phys. Lett. **94**, 053120 (2009).
[48] A. M. Weiner, Rev. Sci. Instrum. **71**, 1929 (2000).
[49] M. Spyridaki, E. Koudoumas, P. Tzanetakis, C. Fotakis, R. Stoian, A. Rosenfeld, and I. V. Hertel, Appl. Phys. Lett. **83**, 1474 (2003).
[50] T. Gunaratne, M. Kangas, S. Singh, A. Gross, and M. Dantus, Chem. Phys. Lett. **423**, 197 (2006).
[51] M. Guillermin, C. Liebig, F. Garrelie, R. Stoian, A. S. Loir, and E. Audouard, Appl. Surf. Sci. **255**, 5163 (2009).
[52] B. J. Garrison, T. E. Itina, and L. V. Zhigilei, Phys. Rev. E **68**, 041501 (2003).
[53] P. Lorazo, L. J. Lewis, and M. Meunier, Phys. Rev. B **73**, 134108 (2006).
[54] R. S. Judson and H. Rabitz, Phys. Rev. Lett. **68**, 1500 (1992).
[55] A. Assion, T. Baumert, M. Bergt, T. Brixner, B. Kiefer, V. Seyfried, M. Strehle, and G. Gerber, Science **282**, 919 (1998).
[56] C. Daniel, J. Full, L. González, C. Lupulescu, J. Manz, A. Merli, S. Vajda, and L. Wöste, Science **299**, 536 (2003).
[57] A. Lindinger, C. Lupulescu, M. Plewicki, F. Vetter, A. Merli, S. M. Weber, and L. Wöste, Phys. Rev. Lett. **93**, 033001 (2004).
[58] R. Stoian, A. Mermillod-Blondin, N. M. Bulgakova, A. Rosenfeld, I. V. Hertel, M. Spyridaki, E. Koudoumas, P. Tzanetakis, and C. Fotakis, Appl. Phys. Lett. **87**, 124105 (2005).
[59] H. Dachraoui and W. Husinsky, Phys. Rev. Lett. **97**, 107601 (2006).
[60] X. Zhu, T. C. Gunaratne, V. V. Lozovoy, and M. Dantus, Opt. Express **15**, 16061 (2007).
[61] R. Hergenröder, M. Miclea, and V. Hommes, Nanotechnology **17**, 4065 (2006).
[62] J. M. Liu, Opt. Lett. **7**, 196 (1982).
[63] S. Nolte, C. Momma, H. Jacobs, A. Tünnermann, B. N. Chichkov, B. Wellegehausen, and H. Welling, J. Opt. Soc. Am. B **14**, 2716 (1997).
[64] M. Hashida, A. F. Semerok, O. Gobert, G. Petite, and J.-F. Wagner, Proc. SPIE **4423**, 178 (2001).
[65] A. R. Striganov and N. S. Sventitskii, *Tables of Spectral Lines of Neutral and Ionized Atoms* (IFI/Plenum, New York, Washington, 1968).
[66] The previous reported line of Al-II at 618.157 and 618.168 nm in Ref. 51 is not considered anymore. This transition was previously associated with an Al-II line at 618.157 nm which was presenting an anomalous behavior. It is conceivable that we observe the Fe-I transitions at 618.02 or 618.799 nm.
[67] A. V. Bushman, I. V. Lomonosov, and V. E. Fortov, Sov. Technol. Rev. B **5**, 1 (1993).
[68] J. P. Colombier, P. Combis, R. Stoian, and E. Audouard, Phys. Rev. B **75**, 104105 (2007).
[69] E. Palik, *Handbook of Optical Constants of Solids* (Academic Press, London, 1985).
[70] W. Ebeling, A. Förster, V. Fortov, V. Griaznov, and A. Polishchuk, *Thermophysical Properties of Hot Dense Plasmas* (Teubner, Stuttgart, 1991).
[71] L. Spitzer, *Physics of Fully Ionized Gases* (Interscience, New York, 1967).
[72] J. P. Colombier, P. Combis, E. Audouard, and R. Stoian, Phys. Rev. E **77**, 036409 (2008).
[73] S. I. Anisimov, B. L. Kapeliovich, and T. L. Perel'man, Sov. Phys. JETP **39**, 375 (1974).
[74] Z. Lin, L. V. Zhigilei, and V. Celli, Phys. Rev. B **77**, 075133 (2008).
[75] D. O. Gericke, M. S. Murillo, and M. Schlanges, Phys. Rev. E **65**, 036418 (2002).
[76] J. Daligault and D. Mozyrsky, Phys. Rev. E **75**, 026402 (2007).
[77] http://www.t4.lanl.gov/opacity/tops.html
[78] N. H. Magee, Jr., J. Abdallah, Jr., R. E. H. Clark *et al.*, *Astrophysical Applications of Powerful New Databases*, Astronomical Society of the Pacific Conference Series Vol. 78, edited by S. J. Adelman and W. L. Wiese (Astronomical Society of the Pacific, San Francisco, 1995), p. 51.
[79] D. K. Kim and I. Kim, Phys. Rev. E **68**, 056410 (2003).
[80] C. Aragòn and J. A. Aguilera, Spectrochim. Acta, Part B **63**, 893 (2008).
[81] J. A. Aguilera and C. Aragòn, Spectrochim. Acta, Part B **59**, 1861 (2004).
[82] X. Wang, S. Amoruso, and J. Xia, Appl. Surf. Sci. **255**, 5211 (2009).
[83] S. Laville, F. Vidal, T. W. Johnston, M. Chaker, B. Le Drogoff, O. Barthelemy, J. Margot, and M. Sabsabi, Phys. Plasmas **11**, 2182 (2004).
[84] N. M. Bulgakova, A. V. Bulgakov, and O. F. Bobrenok, Phys. Rev. E **62**, 5624 (2000).
[85] A. Miotello and R. Kelly, Appl. Phys. Lett. **67**, 3535 (1995).
[86] B. J. Siwick, J. R. Dwyer, R. E. Jordan, and R. J. Dwayne Miller, Science **302**, 1382 (2003).
[87] M. Kandyla, T. Shih, and E. Mazur, Phys. Rev. B **75**, 214107 (2007).
[88] M. Guillermin, A. Klini, J. P. Colombier, F. Garrelie, D. Gray, C. Liebig, E. Audouard, C. Fotakis, and R. Stoian, Opt. Express **18**, 11159 (2010).
[89] A. V. Bulgakov, I. Ozerov, and W. Marine, Thin Solid Films **453-454**, 557 (2004).
[90] A. K. Upadhyay and H. M. Urbassek, Phys. Rev. B **73**, 035421 (2006).
[91] T. E. Glover, J. Opt. Soc. Am. B **20**, 125 (2003).
[92] T. E. Glover, G. D. Ackerman, A. Belkacem, P. A. Heimann, Z. Hussain, R. W. Lee, H. A. Padmore, C. Ray, R. W. Schoenlein, W. F. Steele, and D. A. Young, Phys. Rev. Lett. **90**, 236102 (2003).
[93] B. Chimier and V. T. Tikhonchuk, Phys. Rev. B **79**, 184107 (2009).
[94] K. Sokolowski-Tinten, J. Bialkowski, A. Cavalleri, D. von der Linde, A. Oparin, J. Meyer-ter-Vehn, and S. I. Anisimov, Phys. Rev. Lett. **81**, 224 (1998).
[95] N. Inogamov, Y. Petrov, S. Anisimov, A. Oparin, N. Shaposhnikov, D. von der Linde, and J. Meyer-ter-Vehn, JETP Lett. **69**, 310 (1999).
[96] J. P. Colombier, E. Audouard, P. Combis, A. Rosenfeld, I. V. Hertel, and R. Stoian, Appl. Surf. Sci. **255**, 9597 (2009).
[97] J. E. Jensen, W. A. Tuttle, R. B. Stewart, H. Brechna, and A. G. Prodell, *Brookhaven National Laboratory Selected Cryogenic Data Notebook* (Brookhaven National Laboratory, New York, 1980).